



Cite this: *Mater. Adv.*, 2022, 3, 5163

Cu₃N/Cu₂O core–shell nanowires: growth and properties†

Kalliopi Mavridou,^{ab} Maria Katsikini,^b Andreas Othonos,^c Nikoletta Florini,^a Philomela Komninou^a and Matthew Zervos^{b*}^d

CuO nanowires with diameters between 100 and 200 nm, lengths up to ~ 10 μm and a uniform distribution have been grown at 600 $^{\circ}\text{C}$ under 100 mL min^{-1} O₂ on 15 mm \times 30 mm Cu foils. The CuO nanowires have a monoclinic crystal structure, grow by a vapor–solid mechanism and can be reduced to Cu under H₂ at 300 $^{\circ}\text{C}$ but they are shortened, contain residual Cu₂O and are eliminated above 400 $^{\circ}\text{C}$. We develop a strategy to preserve their integrity via the deposition of Cu over the CuO in order to convert them into Cu₃N under NH₃:H₂. The Cu₃N nanowires obtained in this way are curly and have a cubic anti-ReO₃ crystal structure but are surrounded by a surface shell of Cu₂O with a thickness of a few tens of nm as shown by transmission electron microscopy. We find that the CuO NWs coated with Cu having a thickness greater than 200 nm are not fully converted into Cu₃N and have an inner core of CuO. The Cu₃N nanowires exhibited four maxima in differential transmission at 2.41, 2.17, 1.9 and 1.8 eV, using ultrafast absorption-transmission spectroscopy, corresponding to the M and R direct energy band gaps of Cu₃N in good agreement with theory but we find no evidence for quantization. In addition, we observed two minor peaks at 1.69 and 1.67 eV that may be related to transitions between states in the Cu₂O shell or Cu₃N under compression. Despite the fact that Cu₃N has no mid-gap states the photo-generated carriers have lifetimes less than 100 ps, so its potential as a defect tolerant semiconductor for energy conversion is discussed along with its perspective for energy storage.

Received 8th February 2022,
Accepted 16th May 2022

DOI: 10.1039/d2ma00140c

rsc.li/materials-advances

1. Introduction

Cu₃N¹ is a binary semiconductor with an indirect energy band gap of 1.0 eV that has a cubic a-ReO₃ crystal structure with a lattice constant of 3.8 \AA (space group *PM*³*m*, Number 221).² It has been described as a defect tolerant semiconductor which is the tendency of a semiconductor to keep its properties despite the presence of crystallographic defects as suggested by Zakutayev *et al.*³ As such it has been proposed to be used as a solar cell absorber considering that bipolar doping is possible³ but also for energy storage and the realization of batteries⁴ due to the large voids in the center of its cubic structure that can accommodate foreign atoms, such as lithium.⁵ It has been found that Li_{3-x}Cu_xN has a high reversible capacity of 650 mA h g⁻¹ so Cu₃N is indeed an attractive material for energy storage and Lithium-ion

batteries (LIB)^{6,7} but so far no one has fabricated a solar cell device using Cu₃N exhibiting photovoltaic action.

In the past, Cu₃N layers have been prepared by a variety of methods including, sputtering,⁸ molecular beam epitaxy,⁹ atomic layer deposition^{10,11} and pulsed laser deposition^{12,13} but in most cases Cu₃N has been obtained by sputtering under Ar and N₂. For instance, Birkett *et al.*⁸ prepared Cu₃N by sputtering under Ar and N₂ and the direct energy band gap was found to be 1.68 eV at 300 K which increased very slightly up to 1.7 eV at 4.2 K consistent with their electronic structure calculations. Recently, Matsuzaki *et al.*¹⁴ obtained Cu₃N directly from Cu under NH₃ and O₂ at temperatures ranging between 500 $^{\circ}\text{C}$ and 800 $^{\circ}\text{C}$. The conversion of Cu into Cu₃N was suggested to occur via a two-step reaction of Cu with O₂ and then with NH₃ which in a way is similar to the conversion of Ga₂O₃ nanowires into GaN under NH₃ at elevated temperatures.¹⁵

In the past only, a few have investigated the growth and properties of Cu₃N nanowires (NWs). More specifically Wang *et al.*¹⁶ prepared Cu₃N NWs by forming Cu(OH)₂ NWs on Cu foils that were subsequently exposed to NH₃ at 350 $^{\circ}\text{C}$ for 3 h. In addition, Ma *et al.*¹⁷ observed the formation of a planar network of sub-nm diameter Cu₃N NWs on Cu(110) foils by strain relief guided growth under N₂ at 10⁻⁷ mbar and 427 $^{\circ}\text{C}$. Moreover, Zhang *et al.*¹⁸ obtained Cu₃N rods by metal organic chemical

^a School of Physics, Aristotle University of Thessaloniki, GR-54124, Thessaloniki, Greece. E-mail: zervos@ucy.ac.cy

^b Helmholtz-Zentrum Dresden-Rossendorf, PO Box 01328, Dresden, Germany

^c Laboratory of Ultrafast Science, University of Cyprus, Nicosia, PO Box 20537, Nicosia, 1678, Cyprus

^d Nanostructured Materials and Devices Laboratory, School of Engineering, University of Cyprus, PO Box 20537, Nicosia, 1678, Cyprus

† Electronic supplementary information (ESI) available. See DOI: <https://doi.org/10.1039/d2ma00140c>



vapor deposition (MOCVD) using copper(II) acetylacetone with H_2NH_3 while Hou *et al.*¹⁹ investigated the electrical properties of $\text{Ni}-\text{Cu}_3\text{N}$ NWs and used them for water splitting. More recently, Cu_3N NWs were prepared by the formation of $\text{Cu}(\text{OH})_2$ NWs on Cu foils after which they were converted into Cu_3N under a flow of NH_3 . Following this, $\text{Li}_3\text{N}/\text{Cu}$ NWs were obtained by bringing the Cu_3N NWs into contact with Li .²⁰ Lastly, Cu_3N NWs have also been obtained *via* an ammonolysis reaction of copper oxide films.²¹

Here, we have investigated the growth and conversion of CuO into Cu_3N NWs. CuO NWs have been obtained in the past mainly *via* the thermal oxidation of Cu in air or under O_2 due to the inherent simplicity of this method.²² Interestingly, a detailed investigation into the growth of CuO NWs on different Cu surfaces was carried out recently by Popovski *et al.*²³ confirming that CuO NWs may be obtained on Cu foils at temperatures as low as 250 °C. The growth of CuO NWs on Cu foils has also been achieved at low temperatures between 250 °C and 450 °C by Gulbransen *et al.*²⁴ On the other hand, it has been shown by Liang *et al.*²⁵ that the growth of CuO NWs depends on the annealing temperature and the grain size of the Cu foil that is used as substrate. A smaller grain size and single grain orientation can produce longer, denser and a more uniform distribution of CuO NWs. However, a significant disadvantage of the CuO NWs obtained *via* the thermal oxidation of Cu foils is that intermediate layers of CuO and Cu_2O are formed so a significant lattice mismatch exists between the Cu, CuO and Cu_2O which in turn makes the CuO NW network particularly fragile. Nevertheless, it has been shown that the integrity of the CuO NWs can be improved by texturing the surface of the Cu foil.²⁶ It is interesting to point out here that CuO NWs have been used in dye sensitized solar cells,²⁷ sensors,^{28–31} as well as for catalysis³² so the growth, properties and applications of CuO NWs is an ongoing topic of active investigation which is interesting from a fundamental and technological point of view.³³

To the best of our knowledge, no one has investigated previously the conversion of CuO into Cu_3N NWs under NH_3 ; H_2 which is similar to our earlier investigations on the conversion of Ga_2O_3 into GaN NWs under NH_3 at elevated temperatures.¹⁵ We have investigated the structural properties of the CuO and Cu_3N NWs by X-ray diffraction, transmission and scanning electron microscopy as well as Raman spectroscopy. In addition, we have carried out ultrafast pump-probe spectroscopy (UPPS) which is a versatile tool for understanding the generation-recombination, mechanisms and pathways, of photo generated electron-holes that depend on the electronic band structure and energetic position of sub-band gap states related to crystal imperfections and impurities that can't be determined by steady state UV-vis absorption-transmission spectroscopy.

2. Materials and methods

Initially square foils of 10 mm × 10 mm Cu (99.9%) with a thickness of ~0.15 mm or 150 µm were immersed in a solution of HCl and De-ionized (DI) H_2O (1:1) to remove the native

oxide. Subsequently the foils were rinsed with DI water, dried with nitrogen and pressed flat. The growth of CuO NWs on the Cu foils was carried out in a 1" hot wall, horizontal, chemical vapor deposition (CVD) reactor, capable of reaching 1100 °C that was fed on the upstream side by a manifold consisting of four mass flow controllers connected to Ar, NH_3 , O_2 and H_2 . The Cu foil was loaded in a quartz boat that was inserted in the reactor after which it was purged with 500 mL min^{-1} of Ar for 10 min at 1 bar. Then the temperature was ramped at 10 °C min⁻¹ under a flow of 300 mL min^{-1} O_2 up to 600 °C. Upon reaching 600 °C the same flow of O_2 was maintained for 120 min. In order to prevent the development of thermal stress in the Cu foil, the cooling rate was adjusted to 5 °C min⁻¹. The conversion of CuO into Cu_3N NWs was carried out in the temperature range of 300–400 °C for 60 min under a flow of (a) NH_3 (b) $\text{NH}_3\text{:H}_2$ and (c) $\text{NH}_3\text{:O}_2$ after purging with 500 mL min^{-1} of Ar for 10 min. In all cases the samples were removed from the reactor at room temperature.

The morphology and crystal structure of the Cu_3N NWs were determined by Scanning Electron Microscopy (SEM, TESCAN) operated at an accelerated voltage of 30 kV and X-ray diffraction (XRD, Rigaku Co) using Cu K α radiation ($\lambda = 1.54056$ Å) with θ –2 θ mode ranging from 10 to 80°. Transmission Electron Microscopy (TEM) and high-resolution TEM (HRTEM) observations were carried out in a JEOL JEM F200 CFEG TEM/STEM electron microscope operated at 200 kV (point resolution 0.19 nm). TEM samples were prepared by mechanically rubbing the CuO and $\text{Cu}_3\text{N}/\text{Cu}_2\text{O}$ NWs onto TEM carbon coated copper grids. Raman Spectroscopy (RS) was carried out using a DILOR-XY spectrometer equipped with an optical microscope and a 100× objective; the Raman measurements were performed in the backscattering geometry. The red line ($\lambda = 647.1$ nm) of a Kr^+ laser was used for excitation and the spectra were calibrated with a Ne lamp. The power on the sample was less than 2 mW.

Finally, the optical properties of the Cu_3N NWs were investigated by measuring the time evolution of the differential transmission (dT/T) on a ps time scale by UPPS using a pump with $\lambda_{\text{PU}} = 400$ or 260 nm and diameter of 1 mm on the sample and a probe that was varied between $\lambda_{\text{PR}} = 450$ nm and 750 nm. In this case the CuO NWs were removed from the Cu foil by sonication in isopropanol and dispersed gradually on fused silica (f-SiO₂) after which they were converted into Cu_3N under $\text{NH}_3\text{:H}_2$ at 400 °C. UPPS was carried out using a Ti: Sapphire ultrafast amplifier system generating 100 fs pulses at 800 nm and running at a repetition rate of 1 kHz. A nonlinear crystal was used to generate 400 nm for the purpose of exciting the sample, whereas part of the fundamental was used to generate a super continuum light for probing different energy states. The measurements were carried out using a typical pump-probe optical setup in a non-collinear configuration, where the probe beam was directed into a spectrometer with 0.5 nm spectra resolution equipped with a fast CCD array.

3. Results and discussion

3.1 Growth of CuO nanowires on Cu foil

In the past, we have obtained CuO NWs by the thermal oxidation of a Cu foil with a thickness of ~0.15 mm.³⁴ More specifically,



the CuO NWs were obtained in a 1" hot wall reactor that was purged with Ar for 10 min after which the temperature was ramped to 600 °C using a slow ramp rate of 5 °C min⁻¹ and a flow of 100 mL min⁻¹ O₂ that was maintained up to 4 h at 600 °C. The CuO NWs obtained in this way were straight with diameters of ~100 nm, had lengths of up to ~10 µm and exhibited clear peaks in the XRD corresponding to the monoclinic crystal structure of CuO but additional peaks were also observed corresponding to the underlying Cu₂O and Cu foil.

Here, we have grown again CuO NWs on Cu foils at 600 °C for 120 min in order to convert them into Cu₃N NWs by thermal nitridation. A typical SEM image of the Cu foils used for the growth of the CuO NWs is shown in Fig. 1(a). This exhibited well resolved peaks in the XRD as shown in Fig. 1(b) corresponding to the face centered cubic (fcc) crystal structure of Cu with a lattice constant of 3.597 Å. A cross-section of the Cu foil is also shown as an inset in Fig. 1(a), from which we find that it has a thickness of about 120 µm. The CuO NWs that were grown on the Cu foil have diameters of ~100–200 nm, lengths of ~3–10 µm and form a dark black network with excellent uniformity across areas up to 15 × 30 mm. A typical SEM image of the CuO NWs is shown in Fig. 1(c). In fact, the CuO NWs grow on top of a bilayer of bulk CuO and Cu₂O over the Cu foil.

A reduction of about 40 µm in the thickness of the Cu foil occurred after growth as shown in Fig. 1(d). The CuO NWs exhibited well resolved peaks in the XRD pattern as shown in Fig. 1(e) corresponding to the monoclinic crystal structure of CuO and also a few peaks due to the Cu₂O.

A typical TEM image of the CuO NWs is illustrated in Fig. 2(a). They have a straight morphology with averaged projected diameters measured as $d = 150 \pm 30$ nm. The corresponding selected area electron diffraction (SAED) pattern recorded along the [111] zone axis (z.a), shown in Fig. 2(b), confirms the base-centered monoclinic crystal structure of the CuO NWs. The 112, 110 and 202 reflections corresponding to the interplanar spacing (*d*-spacing) of the lattice planes are indicated. A HRTEM image from the surface of a CuO NW is presented in Fig. 2(c). A magnified image of the area bounded by the white frame is given as inset. The lattice fringe spacing, equal to 0.187 nm, corresponds to the *d*-spacing of the (202) lattice planes of the CuO monoclinic structure.

For completeness it should be mentioned that the CuO NWs grow by a vapor–solid (VS) mechanism whereby Cu diffuses out of the underlying foil and oxygen diffuses inwards along grain boundaries, as illustrated in Fig. 1(f). An extensive description of the growth conditions and their optimization as well as

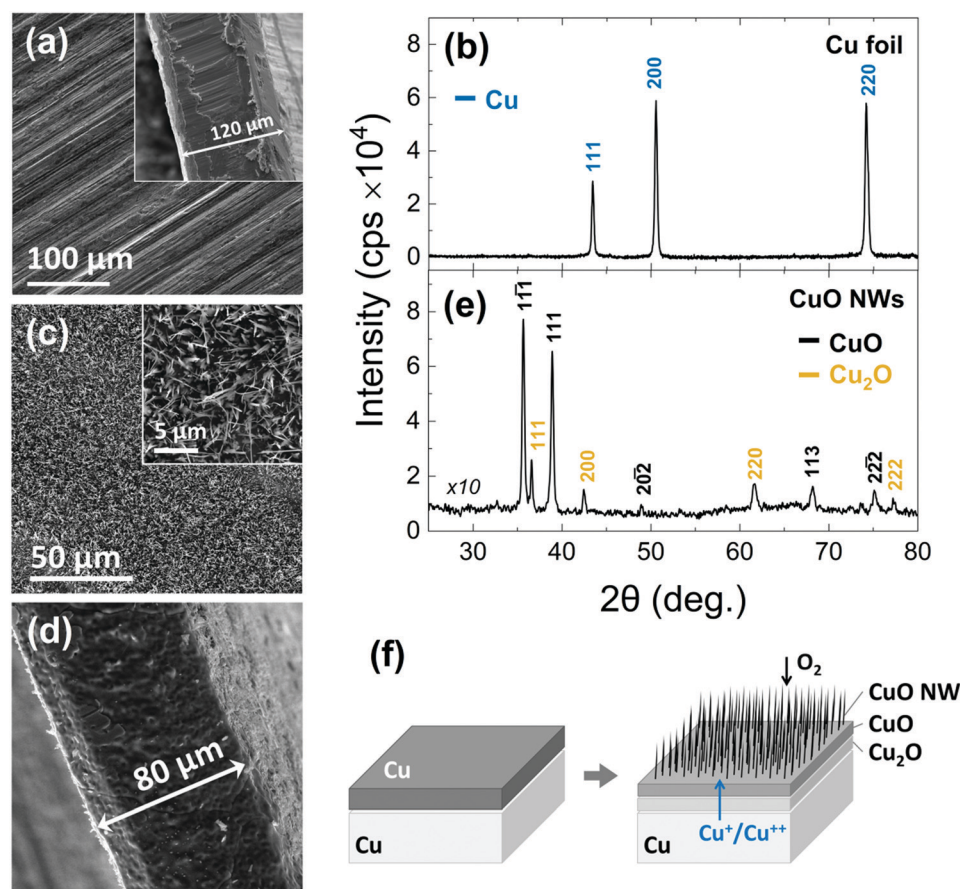


Fig. 1 Growth of CuO NWs. (a) SEM image and (b) XRD pattern of the Cu foil that was used for the growth of the CuO NWs. (c) SEM image of the CuO NWs that grow on top of the Cu foil (d) Cross-section image of the Cu foil after removing the bulk CuO layer and CuO NWs (e) XRD pattern of the CuO NWs after being removed from the underlying Cu foil (f) schematic illustration of the growth of CuO NWs.



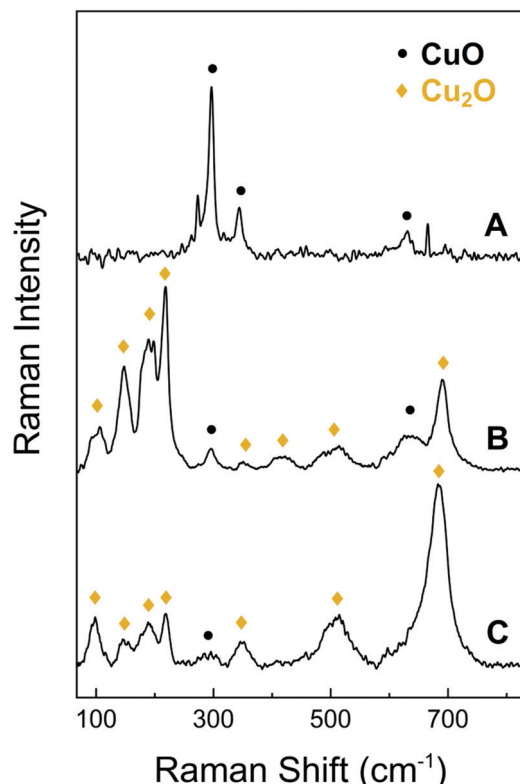


Fig. 2 Raman spectra of the CuO NWs (A), the bulk CuO layer that supports the CuO NWs after being detached from the underlying foil (B) and the surface of the bare Cu foil (C).

issues pertaining to the integrity of the CuO NW network is provided in the ESI,† S1.

In addition to the above, we investigated the structural properties of the CuO NWs by Raman spectroscopy and found that the conversion of the Cu to CuO NWs occurs gradually, from Cu to Cu₂O and then to CuO. As expected, it is found that the CuO NWs consist only of CuO phase, as shown by trace A of Fig. 3. The Raman line observed at 290 cm⁻¹ can be attributed to the A_g mode and the 345 and 630 cm⁻¹ peaks to the B_g modes of the CuO phase.³⁵ The bulk layer supporting the CuO NWs contains both the CuO and Cu₂O phases as indicated by trace B in Fig. 3. The peak observed at approximately 515 cm⁻¹

can be assigned to the only Raman active mode T_{2g} of Cu₂O. The peaks at 110 cm⁻¹ (E_u), 150 cm⁻¹ (T_{1u}) and 350 cm⁻¹ (A_{2u}) are observed as well and again these are attributed to the Cu₂O phase. Additional features at 220 cm⁻¹ (2E_u), in the vicinity of 400–450 cm⁻¹ and at 695 cm⁻¹ are due to multiphonon Raman scattering. Moreover, the signal observed at 190 cm⁻¹ is attributed to local vibrations of Cu on O-sites.^{36,37} The surface of the Cu foil after the exfoliation of the CuO NWs had a dark red color due to the presence of the Cu₂O phase as shown by trace C in Fig. 3; a minor contribution of CuO was also detected.

In short, a uniform distribution of crystalline CuO NWs over 15 × 30 mm Cu foils was obtained. The CuO NWs are straight, have diameters of 150 ± 30 nm, lengths of ~3–10 μm, a monoclinic crystal structure and do not contain any Cu₂O or Cu.

3.2 Nitridation of CuO into Cu₃N Nanowires

Initially we tried to reduce the CuO into Cu NWs under H₂ in order to subsequently convert them into Cu₃N NWs under NH₃:O₂ similar to the Cu₃N layers that were obtained previously from Cu under NH₃:O₂.³⁸ We find that the CuO NWs can be reduced to Cu under H₂ at 300 °C but contain residual Cu₂O and are shortened. The CuO NWs were eliminated above 400 °C, see ESI,† S2. We developed a strategy to preserve their integrity of the CuO NWs under reducing conditions *via* the deposition of a Cu shell over the CuO NWs in order to convert them into Cu₃N under NH₃:H₂. More specifically Cu with a thickness of 240 nm was deposited on the CuO NWs and the CuO/Cu core-shell NWs were annealed at 400 °C for 60 min under 300:10 mL min⁻¹ NH₃:H₂, as illustrated in Fig. 4(a). The CuO/Cu core-shell NWs maintained their integrity and were converted into Cu₃N NWs that acquired a curly shape as shown in Fig. 4(b) and exhibited well resolved peaks in the XRD pattern belonging to Cu₃N as well as a single peak of low intensity at $2\theta = 77.4^\circ$ which may be indexed to the (222) crystallographic plane of the monoclinic crystal structure of Cu₂O as shown in Fig. 4(c). The Cu₃N phase was also identified by the major peaks of the optical modes T_{2u} (170 cm⁻¹) and T_{1u} (655 cm⁻¹),³⁹ in the Raman spectra shown in Fig. 4(d). A smaller contribution of the Cu₂O phase, with peaks at *ca.* 150 and 220 cm⁻¹ is also detected. For comparison, the Raman spectrum recorded from a Cu₃N thin film obtained from

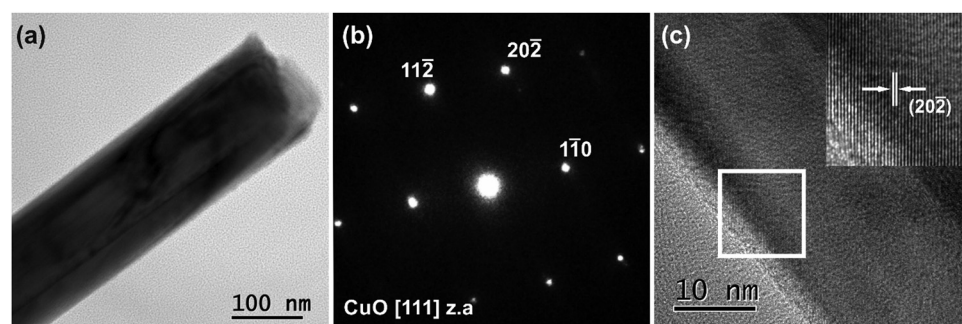


Fig. 3 (a) TEM image of a CuO NW along with (b) the corresponding SAED pattern recorded along the [111] zone axis of monoclinic CuO. (c) HRTEM image showing the edge side of a CuO NW and as inset, magnification of the area in the rectangle frame indicating the spacing of the (202) lattice fringes of CuO.



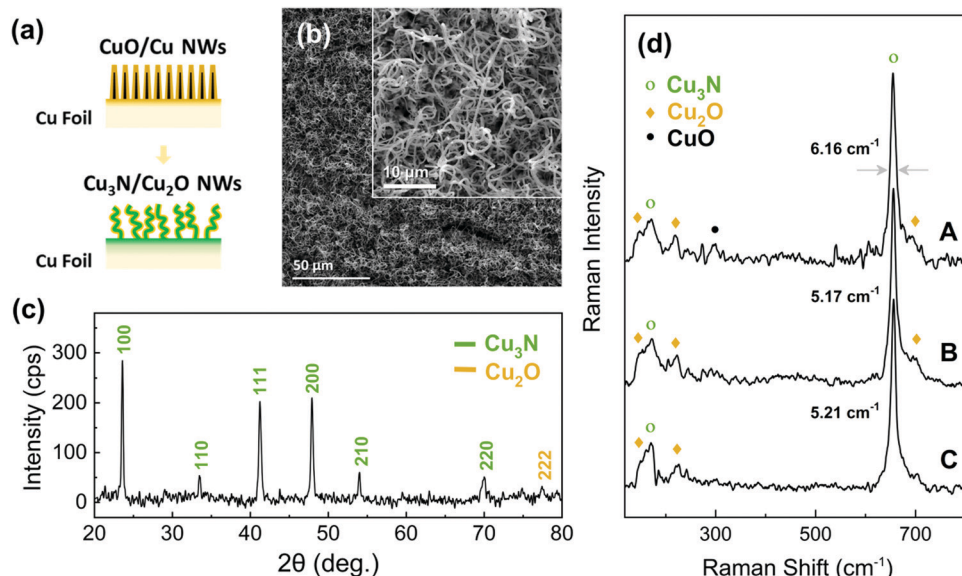


Fig. 4 (a) Schematic illustration of the conversion of the CuO into Cu₃N NWs (b), (c) SEM image and XRD pattern of the Cu₃N/Cu₂O NWs obtained from the CuO NWs that were coated with 240 nm Cu (d) Raman spectra of the Cu₃N/Cu₂O NWs obtained from CuO NWs that were coated with 480 nm Cu (trace A) and 240 nm Cu (trace B) and treated under NH₃: H₂; also shown the case of a Cu₃N thin film obtained from a 240 nm Cu layer that was deposited on a Cu foil and treated under NH₃: H₂ (trace C).

annealing of a Cu foil under NH₃:H₂ flow is shown at the bottom of Fig. 4(d). The Cu₂O phase is also detected in this case and can be attributed to the surface native oxide of Cu₃N. It is worth noting that the CuO NWs covered with a 480 nm Cu shell that were converted into Cu₃N still contained CuO as shown in Fig. 4(d). This can be attributed to the incomplete conversion of the CuO NWs to Cu₃N due to the fact that the oxygen atoms had to travel a longer distance in order to out-diffuse from the core during the nitridation process. Moreover, the peak at *ca.* 655 cm⁻¹ for the Cu₃N NWs obtained from CuO NWs covered with a Cu shell of 480 nm is broader compared to that of the Cu₃N NWs, obtained from CuO NWs covered with a thin shell of 240 nm, indicating a decrease in crystallinity.

In order to gain a deeper insight, the structural properties of the Cu₃N NWs were investigated by TEM. A curly like morphology with rough side surfaces was observed, as shown in Fig. 5(a). The Cu₃N NWs had a diameter $d = 320 \pm 35$ nm. The strong

diffraction contrast of the image revealed that the Cu₃N NWs actually consist of a CuO core with an averaged projected diameter of 40 ± 5 nm. Detailed SAED analysis demonstrated that the Cu₃N NWs are polycrystalline as confirmed by the ring SAED pattern shown in Fig. 5(b). The indexed rings, originating from misoriented crystallites, correspond to the interplanar spacing of 110, 111, 200, 210, 220 and 311 lattice planes of the cubic anti-*ReO*₃ structure of Cu₃N. In the SAED pattern of Fig. 5(b) two additional rings were detected assigned to the interplanar spacing of 111 and 211 planes of the cubic Cu₂O. The presence of Cu₂O has been also confirmed by HRTEM observations. An HRTEM image recorded near the side surface of the Cu₃N/Cu₂O NW is presented in Fig. 5(c), while a magnification of the area in the rectangular frame (given as inset) illustrates its atomic structure, projected along the [110] z.a. of the cubic Cu₂O. The viewing direction is also confirmed by the corresponding FFT (2nd inset), calculated from the HRTEM image, where the 111,

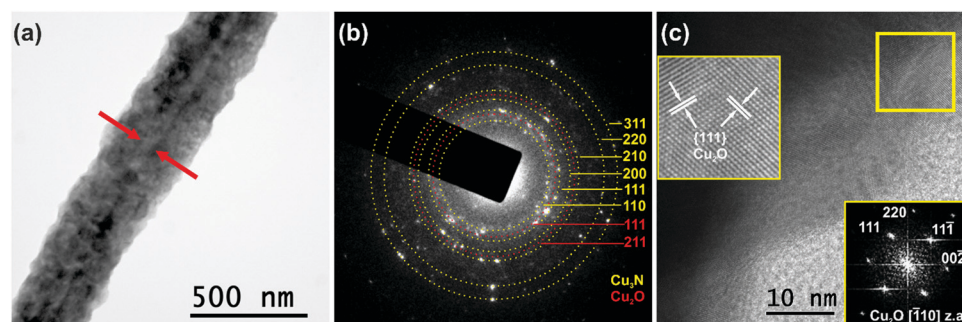


Fig. 5 (a) TEM image of a Cu₂O/Cu₃N core–shell NW; the CuO core is denoted by arrows. (b) Corresponding SAED pattern comprising diffraction rings that correspond to interplanar spacings of the cubic Cu₂O and Cu₃N structures. (c) HRTEM image of the side surface of a Cu₃N/Cu₂O NW; the two insets illustrate the atomic structure of the area in the rectangular frame viewed along the [110] Cu₂O z.a. and the corresponding FFT.



111, 002, 220 spatial frequencies of the [110] z.a. are indicated. Two families of {111} lattice fringes of the cubic Cu₂O are indicated. It is estimated that a 30 nm Cu₂O oxide layer covers the surface of the Cu₃N NWs.

3.3 Ultrafast pump-probe spectroscopy of Cu₃N/Cu₂O NWs

In order to measure the optical properties of the Cu₃N NWs by UPPS we removed CuO NWs from the Cu foil by sonication in isopropanol and dispersed them gradually on transparent fused silica (f-SiO₂) after which they were converted into Cu₃N under NH₃:H₂ at 400 °C as shown in Fig. 6(a). The time evolution of the differential transmission (dT/T) on a ps time scale is shown in Fig. 6(b and c) for different probe wavelengths λ_{PR} that vary between 450 and 750 nm after 'pumping' the Cu₃N NWs with light having a wavelength of $\lambda_{\text{PU}} = 260$ nm and incident energy of 1 and 5 μJ respectively. The incident energy was varied between 1 and 5 μJ to avoid the generation of an overtly high carrier density which leads to a smearing of the spectral structure as we have shown previously.³⁸ In essence the photoexcited electrons will occupy states in the conduction band and recombine over a few tens of ps by moving to states with lower energy, during which the transmission of light with wavelengths that vary between 450 and 750 nm is measured, to find out which states are occupied thereby revealing their energetic position and giving insight into the actual electronic band structure. The Cu₃N NWs exhibited maxima at 515 nm ($\equiv 2.41$ eV), 570 nm ($\equiv 2.17$ eV), 650 nm ($\equiv 1.91$ eV) and

690 nm ($\equiv 1.8$ eV) as measured by UPPS that are shown in Fig. 6(b and c). The lower energy duo of maxima at $\lambda_{\text{PR}} = 650$ nm ($\equiv 1.91$ eV) and 690 nm ($\equiv 1.8$ eV) correspond to the M and R direct energy band gaps of bulk-Cu₃N in good agreement with the electronic structure depicted in Fig. 7(a) while the higher energy maxima at 515 nm ($\equiv 2.41$ eV) and 570 nm ($\equiv 2.17$ eV) correspond to the M* and R* direct gaps of Cu₃N under tensile strain that arise due to the formation of Cu₂O on Cu₃N as shown in Fig. 7(b). The spectral structure shown in Fig. 6(b and c) is very similar to that obtained from Cu₃N layers obtained previously from Cu under a flow of NH₃:O₂ between 400 and 600 °C.³⁸ The Cu₃N layers obtained previously exhibited distinct maxima in differential transmission (dT/T) on a ps time scale at 500 nm ($\equiv 2.48$ eV), 550 nm ($\equiv 2.25$ eV), 630 nm ($\equiv 1.97$ eV) and 670 nm ($\equiv 1.85$ eV). We showed that the maxima at 1.97 eV and 1.85 eV correspond to the M and R direct energy band gaps of bulk Cu₃N in excellent agreement with density functional theory (DFT) calculations of the electronic band structure. This observation of the M and R direct energy band gaps of Cu₃N was possible by virtue of the fact that crystal imperfections, such as N vacancies (V_N), Cu interstitials (Cu_i) etc. give rise to states that are energetically located very close or inside the conduction and valence band edges as shown by Yee *et al.* who investigated the properties of N-rich Cu₃N and confirmed the existence of Cu interstitials (Cu_i) by photo thermal deflection spectroscopy (PDS). The latter is an indirect method with dramatically higher sensitivity than steady state

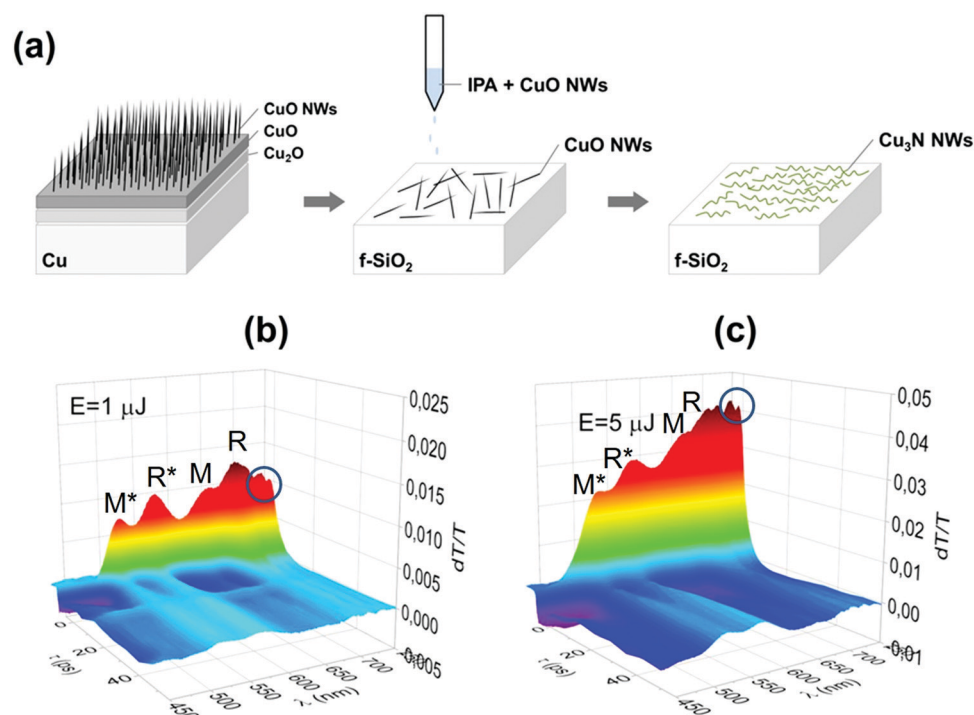


Fig. 6 (a) Schematic illustration of the isolation and conversion of CuO into Cu₃N/Cu₂O NWs. UPPS of Cu₃N/Cu₂O NWs on f-SiO₂ showing the differential transmission dT/T on the vertical axis (no units) versus time delay τ (ps) and probe wavelength λ (nm) for incident energies of (b) $E = 1 \mu\text{J}$ and (c) $E = 5 \mu\text{J}$. The maxima at 515 nm ($\equiv 2.41$ eV), 570 nm ($\equiv 2.17$ eV) correspond to the M* and R* direct band gaps of Cu₃N under tensile strain while those at 650 nm ($\equiv 1.91$ eV) and 690 nm ($\equiv 1.8$ eV) correspond to the M and R bulk band gaps of Cu₃N. The encircled, minor peaks at 730 nm ($\equiv 1.69$ eV) and 740 nm ($\equiv 1.67$ eV) may be attributed to states in Cu₂O or to the M* and R* direct band gaps of Cu₃N under compressive strain.



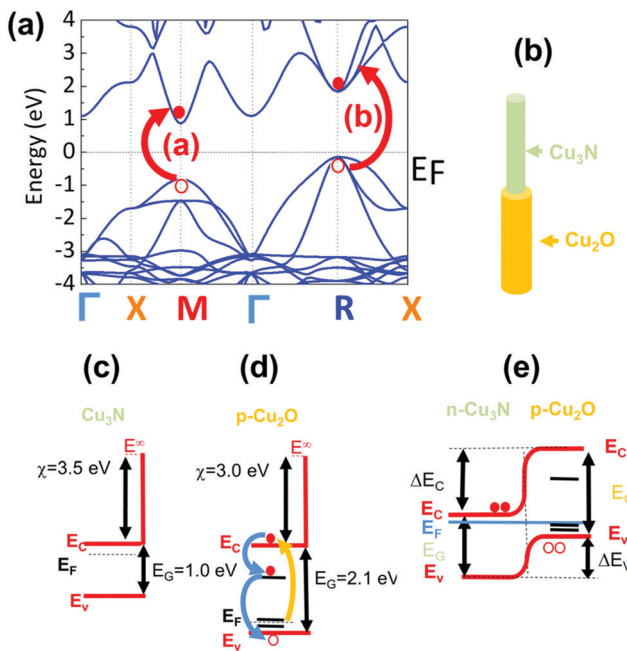


Fig. 7 (a) Electronic structure of Cu_3N showing the excitation of an electron and its transition across the M and R direct energy bandgaps in good agreement with the energetic position of the maxima in differential transmission observed at 1.91 eV and 1.8 eV corresponding to bulk Cu_3N (b) schematic of a $\text{Cu}_3\text{N}/\text{Cu}_2\text{O}$ core–shell NW (c), (d) energy band diagrams of Cu_3N and Cu_2O showing the states at ~ 0.16 eV above E_V and ~ 0.4 eV below E_C (e) energy band diagram of a p–n heterojunction $\text{Cu}_3\text{N}/\text{Cu}_2\text{O}$ core–shell NW.

UV-vis spectroscopy that can be used for the detection of sub-band-gap states that are related to crystal imperfections and/or impurities. In addition, we showed that the maxima at 2.48 eV and 2.25 eV correspond to the M and R direct gaps of certain regions of Cu_3N layers under tensile strain that arise due to the formation of CuO and Cu_2O , *via* the out-diffusion of oxygen from the underlying fused silica (f-SiO₂) and/or surface oxidation.⁴⁰ The spectral structure of the $\text{Cu}_3\text{N}/\text{Cu}_2\text{O}$ NWs shown in Fig. 6(b and c) is similar to that obtained previously from Cu_3N layers³⁸ but we do not observe any quantization effects, as the peaks corresponding to bulk Cu_3N are not blue-shifted to higher energies. However the Cu_3N NWs exhibited peaks at 730 nm ($\equiv 1.69$ eV) and 740 nm ($\equiv 1.67$ eV) shown in Fig. 6(b and c) that were not observed in our previous investigations of Cu_3N layers. The maxima at 730 nm ($\equiv 1.69$ eV) and 740 nm ($\equiv 1.67$ eV) may correspond to the M* and R* direct gaps of the Cu_3N closer to the core that could be under compressive strain. These values are close to those found by Birket *et al.*⁸ who investigated the variation of the energy bandgap with temperature using Fourier transform infra-red spectroscopy. They prepared Cu_3N by sputtering under Ar and N₂ and the direct energy band gap was found to be 1.68 eV at 300 K but changed only very slightly up to 1.7 eV at 4.2 K. However, Birket *et al.*⁸ showed that the direct and indirect band gap changes from 1.4 eV to 2.0 eV and 0.6 eV to 1.8 eV respectively upon increasing the lattice constant from 3.8 Å to 3.9 Å. Consequently, structural distortion has a pronounced

effect on the values of the direct and indirect band-gap and by extension on the optical band gap. This is most likely why there is such a broad variation in the optical band gaps of Cu_3N determined previously by others using steady state optical spectroscopy, *i.e.* UV-vis absorption-transmission, reflectance-transmission spectroscopy, ellipsometry that vary between 1.2 to 2.4 eV.^{41–51} Alternatively, the maxima observed at 730 nm ($\equiv 1.69$ eV) and 740 nm ($\equiv 1.67$ eV) in Fig. 6(b and c) may be related to transitions between states in the Cu_2O shell. It is useful to mention at this point that Cu_2O is a p-type metal-oxide semiconductor that has a direct energy band-gap of 2.1 eV and the Fermi level at the surface is pinned at surface states residing ~ 0.4 eV below the conduction band edge leading to a depletion.⁵² It should also be pointed out that Cu_2O has acceptor like states located ~ 0.16 eV above the valence band maximum that are related to copper vacancies (V_{Cu}) and give rise to its native p-type conductivity.^{40,53} Consequently the maxima observed at 730 nm ($\equiv 1.69$ eV) and 740 nm ($\equiv 1.67$ eV) in Fig. 6(b and c) may be related to transitions between these states that are shown schematically in Fig. 7(d).

The energy band diagram of the $\text{Cu}_3\text{N}/\text{Cu}_2\text{O}$ core–shell NW is shown in Fig. 7(e). We have shown previously that oxygen on nitrogen sites (O_N) have the lowest formation energy and oxygen acts as a donor in Cu_3N .⁴⁰ Consequently, the Cu_3N is expected to be n-type in contrast to CuO and Cu_2O that are p-type, hence the $\text{Cu}_3\text{N}/\text{Cu}_2\text{O}$ core–shell NW is a p–n heterojunction. It should be mentioned that Cu_2O which is the native oxide of Cu_3N was suggested³ that could act in a beneficial way to Cu_3N as a surface passivation layer similar to SiO₂ in Si solar cells. However, the lifetime of the photogenerated electron–hole pairs is of the order of a few tens of ps as shown by the time evolution of the differential transmission in Fig. 6(b and c) which implies that the photoexcited carriers quickly recombine so the idea that Cu_2O may act as a passivation layer for Cu_3N may not be so valid in reality. Finally it should be pointed out that despite the fact that Cu_3N has a “clean bandgap” with no mid gap states and has been described to be a defect tolerant semiconductor that is attractive as a solar cell absorber, no one has so far fabricated a p–n junction solar cell using Cu_3N that exhibits photovoltaic action. In the past, Chen *et al.*⁵⁴ fabricated a p–n Cu_3N homo junction on indium tin oxide (ITO) and Yee *et al.*⁵⁵ fabricated an Al: ZnO/ZnS/ Cu_3N p–n heterojunction both of which showed rectifying behavior, but no photo generated current, attributed to a high density of N vacancies (V_N) and Cu interstitials (Cu_i) that capture electrons and result into significant Shockley–Read–Hall recombination and suppression of the photogenerated electron–hole pairs. So, while crystal defects such as V_N and Cu_i, do not give rise to mid-gap states they still act in a detrimental fashion that hinders the use of Cu_3N as a defect tolerant semiconductor for the fabrication of solar cells. One way of overcoming these difficulties is to grow Cu_3N nanostructures on epitaxial, high crystal quality, transparent conducting oxides *e.g.* Sb: SnO₂ NWs which will permit the extraction of the minority carriers over shorter lengths so that Cu_3N may be used for energy conversion as a solar cell absorber. Nevertheless, the Cu_3N NWs obtained here



that have diameters between 100 and 200 nm and lengths up to $\sim 10 \mu\text{m}$ can be used directly for energy storage as they have a large surface area and can be easily removed and transferred onto a flexible substrate for the purpose of making devices such as supercapacitors or batteries.

4. Conclusions

CuO NWs with diameters of $150 \pm 30 \text{ nm}$, lengths up to $3\text{--}10 \mu\text{m}$ and a uniform distribution have been grown *via* the thermal oxidation of Cu foils at 600°C under O_2 . The CuO NWs have a monoclinic crystal structure and grow by a vapor-solid mechanism on top of bulk CuO and Cu_2O that forms first on top of the Cu foil. We developed a strategy to convert the CuO into Cu_3N NWs under $\text{NH}_3\text{:H}_2$ *via* the deposition of Cu over the CuO NWs in order to maintain their integrity under reducing conditions. The Cu_3N NWs obtained in this way are curly, have a cubic anti- ReO_3 crystal structure but are surrounded by a surface shell of Cu_2O . The CuO NWs with a 480 nm shell of Cu are not converted completely into Cu_3N and consist of a CuO core with thicknesses of a few tens of nm *i.e.* the CuO/ Cu_3N core-shell NWs have an averaged projected diameter $d = 320 \pm 35 \text{ nm}$; $40 \pm 5 \text{ nm}$ for the core.

The Cu_3N NWs exhibited maxima in differential transmission at 2.41, 2.17, 1.9 and 1.8 eV as measured by UPPS that correspond to the M and R direct energy band gaps of Cu_3N but we find no evidence for quantization. In addition, we observed two minor, but well resolved peaks close to the infra-red at 1.69 and 1.67 eV that may be attributed to the M and R direct energy band gaps of Cu_3N under compression or due to recombination *via* states in the Cu_2O . The photogenerated carriers have lifetimes less than 100 ps, so the potential of Cu_3N as a defect tolerant semiconductor-solar cell absorber for energy conversion is currently limited in contrast to that for energy storage.

Conflicts of interest

The author declares no competing interest.

Acknowledgements

P. K. and N. F. acknowledge support by project “INNOVATION-EL” (MIS 5002772), funded by the Operational Programme “Competitiveness, Entrepreneurship and Innovation” (NSRF 2014-2020), co-financed by Greece and the EU (European Regional Development Fund).

References

1. A. Jiang, M. Qi and J. Xiao, *J. Mater. Sci. Technol.*, 2018, **34**, 1467–1473.
2. R. Juza and H. Hahn, *Z. Anorg. Chem.*, 1938, **239**, 282–287.
3. A. Zakutayev, C. M. Caskey, A. N. Fioretti, D. S. Ginley, J. Vidal, V. Stevanovic, E. Tea and S. Lany, *J. Phys. Chem. Lett.*, 2014, **5**, 1117–1125.
4. S. Suwannatus, B. Duangsawat and U. Pakdee, *Mater. Today*, 2018, **5**, 15208–15212.
5. J. Wang, F. Li, X. Liu, H. Zhou, X. Shao, Y. Qu and M. Zhao, *J. Mater. Chem. A*, 2017, **5**, 8762–8768.
6. Y. Yue, P. Han, S. Dong, K. Zhang, C. Zhang, C. Shang and G. Cui, *Chin. Sci. Bull.*, 2012, **57**, 4111–4118.
7. S. Ge, Y. Leng, T. Liu, R. S. Longchamps, X. G. Yang, Y. Gao, D. Wang, D. Wang and C. Y. Wang, *Sci. Adv.*, 2020, **6**, 7633.
8. M. Birkett, C. N. Savory, A. N. Fioretti, P. Thompson, C. A. Muryn, A. D. Weerakkody, I. Z. Mitrovic, S. Hall, R. Treharne, V. R. Dhanak, D. O. Scanlon, A. Zakutayev and T. D. Veal, *Phys. Rev. B*, 2017, **95**, 115201.
9. K. Matsuzaki, T. Okazaki, Y. S. Lee, H. Hosono and T. Susaki, *Appl. Phys. Lett.*, 2014, **105**, 222102.
10. Z. Li and R. G. Gordon, *Chem. Vap. Deposition*, 2006, **12**, 435–441.
11. J. M. Park, K. Jin, B. Han, M. J. Kim, J. Jung, J. J. Kim and W. J. Lee, *Thin Solid Films*, 2014, **556**, 434–439.
12. C. Gallardo-Vega and W. de la Cruz, *Appl. Surf. Sci.*, 2006, **252**, 8001–8004.
13. G. Soto, J. A. Díaz and W. de la Cruz, *Mater. Lett.*, 2003, **57**, 4130–4133.
14. K. Matsuzaki, K. Harada, Y. Kumagai, S. Koshiya, K. Kimoto, S. Ueda, M. Sasase, A. Maeda, T. Susaki, M. Kitano, F. Oba and H. Hosono, *Adv. Mater.*, 2018, **30**, 1801968.
15. A. Othonos, M. Zervos and C. Christofides, *J. Appl. Phys.*, 2010, **108**, 124319.
16. Z. Wang, X. Cao, D. Liu, S. Hao, R. Kong, G. Du, A. M. Asiri and X. Sun, *Chem. – Eur. J.*, 2017, **23**, 4986–4989.
17. X.-D. Ma, D. I. Bazhanov, O. Fruchart, F. Yildiz, T. Yokoyama, M. Przybylski, V. S. Stepanyuk, W. Hergert and J. Kirschner, *Phys. Rev. Lett.*, 2009, **102**, 205503.
18. Y. Zhang, L. Frank Leung-Yuk, Z. Yan and X. Hu, *Sci. China, Ser. E: Technol. Sci.*, 2009, **52**, 352–356.
19. J. Hou, Y. Sun, Z. Li, B. Zhang, S. Cao, Y. Wu, Z. Gao and L. Sun, *Adv. Funct. Mater.*, 2018, **28**, 1803278.
20. D. Lee, S. Sun, J. Kwon, H. Park, M. Jang, E. Park, B. Son, Y. Jung, T. Song and U. Paik, *Adv. Mater.*, 2020, **32**, 1905573.
21. A. Scigala, E. Szłyk, T. Rerek, M. Wiśniewski, L. Skowronski, M. Trzcinski and R. Szczesny, *Materials*, 2021, **14**, 603.
22. X. Jiang, T. Herricks and Y. Xia, *Nano Lett.*, 2002, **2**, 1333–1338.
23. G. Fritz-Popovski, F. Sosada-Ludwikowska, A. Köck, J. Keckes and G. A. Maier, *Sci. Rep.*, 2019, **9**, 807.
24. E. A. Gulbransen, T. P. Copan and K. F. Andrew, *J. Electrochem. Soc.*, 1961, **108**, 119.
25. J. Liang, N. Kishi, T. Soga and T. Jimbo, *J. Nanomater.*, 2011, **2011**, 1–8.
26. H. Yan, X. Xiao, Z. Chen, Y. Chen, R. Zhou, Z. Wang and M. Hong, *Opt. Laser Technol.*, 2019, **119**, 105612.
27. S. Anandan, X. Wen and S. Yang, *Mater. Chem. Phys.*, 2005, **93**, 35–40.
28. D. Li, J. Hu, R. Wu and J. G. Lu, *Nanotechnology*, 2010, **21**, 485502.
29. L. Liao, Z. Zhang, B. Yan, Z. Zheng, Q. L. Bao, T. Wu, C. M. Li, Z. X. Shen, J. X. Zhang, H. Gong, J. C. Li and T. Yu, *Nanotechnology*, 2009, **20**, 085203.



30 O. Lupan, V. Postica, V. Cretu, N. Wolff, V. Duppel, L. Kienle and R. Adelung, *Phys. Status Solidi RRL*, 2016, **10**, 260–266.

31 S. Steinhauer, E. Brunet, T. Maier, G. C. Mutinati, A. Köck, O. Freudenberg, C. Gspan, W. Grogger, A. Neuhold and R. Resel, *Sens. Actuators, B*, 2013, **187**, 50–57.

32 Y. Feng and X. Zheng, *Nano Lett.*, 2010, **10**, 4762–4766.

33 G. Filipič and U. Cvelbar, *Nanotechnology*, 2012, **23**, 194001.

34 A. Othonos and M. Zervos, *Nanoscale Res. Lett.*, 2011, **6**, 622.

35 N. A. Mohammed Shanid, M. Abdul Khadar and V. G. Sathe, *J. Raman Spectrosc.*, 2011, **42**, 1769–1773.

36 B. K. Meyer, A. Polity, D. Reppin, M. Becker, P. Hering, B. Kramm, P. J. Klar, T. Sander, C. Reindl, C. Heiliger, M. Heinemann, C. Müller and C. Ronning, *Semicond. Semimetals*, 2013, 201–226.

37 J. Reydellet, M. Balkanski and D. Trivich, *Phys. Status Solidi B*, 1972, **52**, 175–185.

38 M. Zervos, A. Othonos, M. Sergides, T. Pavloudis and J. Kioseoglou, *J. Phys. Chem. C*, 2020, **124**, 3459–3469.

39 W. Yu, J. Zhao and C. Jin, *Phys. Rev. B: Condens. Matter Mater. Phys.*, 2005, **72**, 214116.

40 M. Zervos, A. Othonos, T. Pavloudis, S. Giaremis, J. Kioseoglou, K. Mavridou, M. Katsikini, F. Pinakidou and E. C. Paloura, *J. Phys. Chem. C*, 2021, **125**, 3680–3688.

41 A. Yu, Y. Ma, A. Chen, Y. Li, Y. Zhou, Z. Wang, J. Zhang, L. Chu, L. Yang and X. Li, *Vacuum*, 2017, **141**, 243–248.

42 K. V. S. Reddy, A. S. Reddy, P. S. Reddy and S. Uthanna, *J. Mater. Sci.: Mater. Electron.*, 2007, **18**, 1003–1008.

43 F. Hadian, A. Rahmati, H. Movla and M. Khaksar, *Vacuum*, 2012, **86**, 1067–1072.

44 T. Maruyama and T. Morishita, *J. Appl. Phys.*, 1995, **78**, 4104–4107.

45 X. M. Yuan, P. X. Yan and J. Z. Liu, *Mater. Lett.*, 2016, **60**, 1809–1812.

46 Y. Hayashi, T. Ishikawa and D. Shimokawa, *J. Alloys Compd.*, 2002, **330–332**, 348–351.

47 G. Sahoo, S. R. Meher and M. K. Jain, *Mater. Sci. Eng., B*, 2015, **191**, 7–14.

48 D. Dorranian, L. Dejam, A. H. Sari and A. Hojabri, *J. Theor. Appl. Phys.*, 2009, **3**, 37–41.

49 Y. Du, A. Ji, L. Ma, Y. Wang and Z. Cao, *J. Cryst. Growth*, 2005, **280**, 490–494.

50 D. M. Borsa and D. O. Boerma, *Surf. Sci.*, 2004, **548**, 95–105.

51 K. J. Kim, J. H. Kim and G. H. Kang, *J. Cryst. Growth*, 2001, **222**, 767–772.

52 J. W. Hodby, T. E. Jenkins, C. Schwab, H. Tamura and D. Trivich, *J. Phys. C: Solid State Phys.*, 1976, **9**, 1429.

53 D. O. Scanlon and G. W. Watson, *J. Phys. Chem. Lett.*, 2010, **1**, 2582.

54 S. C. Chen, S. Y. Huang, S. Sakalley, A. Paliwal, Y. H. Chen, M. H. Liao, H. Sun and S. Biring, *J. Alloys Compd.*, 2019, **789**, 428.

55 Y. S. Yee, H. Inoue, A. Hultqvist, D. Hanifi, A. Salleo, B. Magyari-Köpe, Y. Nishi, S. F. Bent and B. M. Clemens, *Phys. Rev. B*, 2018, **97**, 245201.

